S. Kong
K. Sharif
H. P. Evans
R. W. Snidle
Professor
e-mail: snidler@cf.ac.uk

School of Engineering,
Cardiff University,
CF2 3TA, United Kingdom

Elastohydrodynamics of a Worm Gear Contact

The paper is concerned with prediction of elastic contact and elastohydrodynamic film thickness in worm gears. Using the undeformed geometry of the gap between gear teeth in contact a three-dimensional elastic contact simulation technique has been developed for calculation of the true area of elastic contact under load relative to the wheel and worm surfaces. A parallel investigation of elastohydrodynamic lubrication effects has been carried out using a special non-Newtonian, thermal solver which takes account of the non-symmetrical and spin aspects of worm contacts. An interesting feature of the results obtained is the discovery of regions of poor film forming due to entrainment failure at the edges of the contact. [DOI: 10.1115/1.1308003]

1 Introduction

Worm gears, as shown in Fig. 1, provide a simple and cost-effective solution in power transmission applications where a high reduction ratio is required in relatively slow speed drives. Comparable parallel axis gearing would normally require two or three stages to achieve the same reductions with a consequent increase in complexity and number of parts. Worm drives are widely used in industry for process machinery, conveyors, elevators, etc. The main disadvantages of worm gearing are lubrication and wear problems due to the relatively high degree of sliding at the tooth contacts. In order to avoid scuffing (welding and tearing of the tooth surfaces caused by lubrication breakdown) it has so far been necessary to use metallurgically dissimilar materials for the worm and wheel. Traditionally a steel worm and phosphor (or leaded) bronze wheel are used. Cast iron has also been tried as a wheel material but is generally less resistant to scuffing than bronze. But the use of a relatively soft material for one of the surfaces limits allowable contact stresses and hence load capacity. Existing worm drives therefore tend to have a low power/weight ratio compared to conventional gearing where hardened steel can be used for both contacting surfaces.

The high degree of sliding coupled with unfavorable hydrodynamic conditions lead to relatively low efficiency and poor thermal rating compared to conventional gearing. The mechanical efficiency of typical high ratio designs can be as low as 70–80 percent compared to figures of 95 percent or better for parallel axis units [1]. These well-known drawbacks of worm drives have been tolerated in the past because of their simplicity and low initial cost. In a more competitive gearing world, however, power/weight ratio and thermal rating are becoming more important as selling points, and there is a need to upgrade traditional worm gearing technology with the aim of improving load capacity and efficiency.

Part of the required improvement in worm gearing technology can be made on the basis of a better understanding of the contact geometry and contact stresses and the way in which these are influenced by design, manufacturing accuracy, elastic distortion, and the wear that occurs during operation. This is the subject of tooth contact analysis. Important advances in the understanding of this aspect of worm design have been made recently by, for example, Litvin and Kin [2], Seol and Litvin [3], Fang and Tsay [4], Hu [5], and Su et al. [6]. As a result of improved understanding of geometry it is possible to optimize the design of worm gears having ''localized tooth contact.'' This arrangement introduces a self-aligning point contact between the teeth thus avoiding damaging contact at their edges. The second important aspect of worm gearing is the known, poor elastohydrodynamic lubrication (EHL) performance of the contacts between worm and wheel teeth. The high ratio of sliding to rolling velocity at the contacts combined with what appears to be a relatively unfavorable entraining geometry of typical designs gives poor film-forming characteristics and leads to the main limitations of low load capacity and low efficiency. Of particular interest is the hard steel worm/hard steel wheel combination which is now being considered as a serious alternative to the traditional steel/bronze design as a means of dramatically improving load capacity. Little work appears to have been carried out on detailed modeling of EHL of worm contacts. An early paper by Bathgate and Yates [7] describes the application of elementary line-contact EHL theory to a worm gear together with calculations of flash and total contact temperature. Discharge voltage measurements of film thickness in a worm (which were calibrated in a disk machine) suggested values in the range of 0.03–0.3 μm with the particular oil used. Fuan et al. [8] also applied line contact EHL theory to a worm gear and predicted film thickness values of 0–2.5 μm, and concluded that lubrication in the middle part of the contact area is weak because of poor entertainment conditions in this region. A full thermal EHL model of worm contacts has been published by Simon [9,10]. Results are given in terms of performance curves using nondimensional flash temperature, EHL load carrying capacity, and friction factor ratios. Details of oil film shape and pressure distribution are not shown.

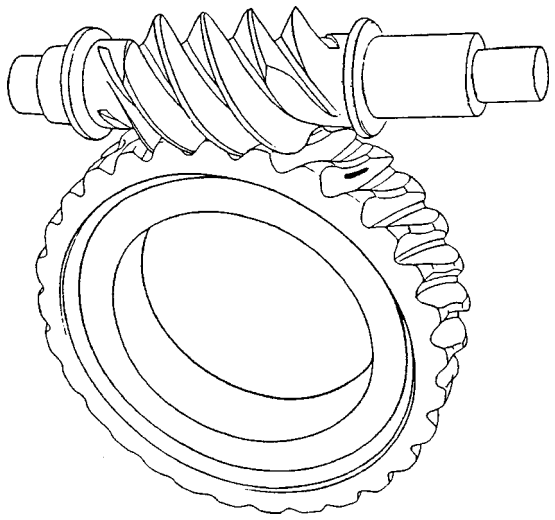

Fig. 1 Worm and wheel pair

Contributed by the Tribology Division of THE AMERICAN SOCIETY OF MECHANICAL ENGINEERS for presentation at the STLE/ASME Tribology Conference, Seattle, WA, October 1–4. Manuscript received by the Tribology Division February 8, 2000; revised manuscript received June 16, 2000. Paper No. 2000-TRIB-15. Associate Editor: J. A. Williams.

One of the aims of the project, of which the present study forms part, is to investigate the geometrical and kinematic design factors which influence hydrodynamic film forming in worms, and to optimize, if possible, these factors in combination with contact stressing and ease of manufacture. Such an integrated approach to improvement of worm gearing technology depends upon a thorough understanding of contact mechanics and hydrodynamic lubrication of the concentrated contacts. The present paper reports on the study of a particular worm gear design over the meshing cycle and the aim is to show the detailed features of the tooth contact in terms of elastostatic and elastohydrodynamic behavior under realistic engineering operating conditions.

2 Geometry and Kinematics of Worm Gears

The worm gears examined in the study so far are of the standard ''ZI'' type. In this system the worm is an involute helicoid. The geometry of the mating wheel is generated from a cutting hob of nominally the same geometry as the worm. In the case where worm and hob are identical, then the meshing action is conjugate with contact occurring at a line, but in order to provide an inlet clearance at the contact to facilitate the generation of an oil film and prevent damaging edge contacts the hob is usually chosen to be ''oversize,'' which means that under unloaded conditions the contact occurs at a point rather than at a line. The process of generation of this nonconjugate geometry of the wheel surface is accomplished by a numerical simulation. A technique for this purpose is described by Hu [5] and is adopted in the present work.

A problem encountered with the numerical data representing the two surfaces was that of precision. Although gap values to the precision produced by the numerical simulation were sufficient for conventional purposes such as transmission error analysis, etc., this led to ''surface roughness'' of sufficient magnitude to give sizeable corresponding ripples in the elastic and EHL pressure distributions in the following elastic and lubrication simulations. While it is recognized that all real engineering surfaces have such features the initial aim of the work was to provide reference solutions to the ideally smooth-surface case. The numerically obtained surfaces were therefore smoothed by fitting high order polynomials to both worm and wheel surfaces. It was found that polynomials of up to order 10 were sufficient to give a very good fit to the surfaces over the whole active part of the teeth. The undeformed gap between the surfaces was then obtained, for each of about 20 meshing positions, by adding the two surface-fitting functions to give an analytical form for the clearance. Contours of this clearance corresponding to a mesh position at which contact occurs roughly half way up the worm tooth are shown in Fig. 2(*a*) for the conjugate case and in Fig. 2(*b*) for an ''oversize'' hob. These latter contours indicate the nonconjugate relative geometry which gives roughly elliptical contours with their major axes aligned nominally across the wheel tooth. The design under consideration is specified by the parameters given in Table 1.

Table 1 Worm/wheel design parameters

Worm tip radius / mm	33.33
Worm root radius / mm	18.78
Worm base radius / mm	8.602
Worm axial pitch / mm	20.94
Worm lead / mm	20.94
Worm base lead angle / degrees	21.18
Number of wheel teeth	40
Wheel face width / mm	46.0
Wheel tip radius / mm	143.23
Wheel throat radius / mm	140.20
Hob tip radius / mm	35.3
Hob root radius / mm	20.8
Hob base radius / mm	8.60
Hob lead / mm	20.94
Hob axial pitch / mm	20.94
Hob base lead angle / degrees	21.18
Hob/wheel centre distance / mm	161.0
Worm/wheel centre distance / mm	160.0

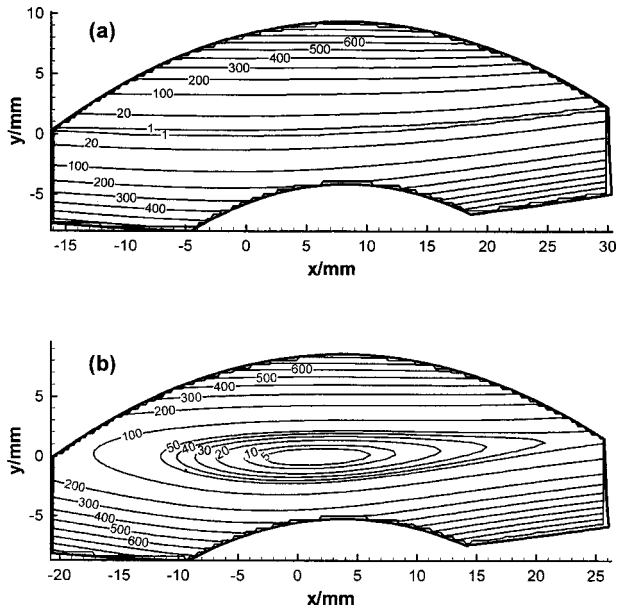

Fig. 2 Wheel tooth showing contours of undeformed gap/μm between worm and wheel teeth (*a*) conjugate case; (*b*) hob oversize case

Kinematical analysis is required for the EHL simulations and corresponding predictions of film forming described below. The velocities of interest are the components of velocity of the two surfaces in the common tangent plane relative to the instantaneous point of contact. This gives the distribution of hydrodynamic entraining, or rolling, velocity in the region of potential contact. The dominant effect is that of the sweeping velocity of the worm surface which gives entrainment mainly in the direction of the major axes of the gap contours. Velocities are obtained by conventional vector methods based on steady rotation of the worm. The instantaneous velocity of the point of contact is obtained by finite differencing positions at successive meshing or ''snapshot'' positions.

3 Elastic Contact Simulation

In simulating elastic contact of the worm teeth the surfaces are assumed to be semi-infinite solids, but the geometry of the gap between undeformed worm teeth in contact is nonsymmetrical so the conventional Hertz equations for the area of contact and contact pressures are only approximations in this case. A numerical method of non-Hertzian elastic contact simulation for nominal point contacts was developed based on the simple method for line two-dimensional (2D) contacts described by Snidle and Evans [11]. The undeformed profiles of the two surfaces are effectively overlapped and from their ''interpenetration'' profile an initial pressure distribution is inferred by suitable scaling. This pressure is then used to calculate elastic deformation of the surfaces and is then adjusted based on the degree of overlap. The process of

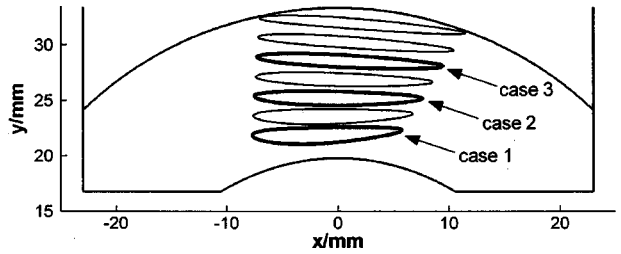

Fig. 3 Dry contact areas at different points within the meshing cycle

pressure adjustment is repeated until the pressure is converged with the overlap equal to zero in the pressurized region. Extension of the technique to the 3D geometry of worm gears is straightforward and simpler in principle because the absolute elastic deformation of the bodies is known, whereas in line contacts deformations are only known to within an undefined constant so that an arbitrary reference point must be taken on the two surfaces. The method was validated before applying it to the worm contacts by obtaining solutions to the known case of elliptical Hertzian contacts over a range of radius ratios.

Results of the elastic contact simulation of the above worm design at different points in the meshing cycle are shown in Fig. 3. In this figure the contact boundaries are projected onto the plane perpendicular to the worm axis so that they may be presented together. The three conditions whose contact boundaries are shown with a heavy line correspond to the cases chosen for EHL analysis in Sec. 5. Figure 4 illustrates the pressure distribution obtained for the central of these three cases which also corresponds to the undeformed geometry illustrated in Fig. 2(*b*).

4 Basic EHL Equations

Worm contacts give rise to an unusual EHL configuration due to the nonsymmetrical geometry and entrainment velocity pattern. Entrainment is dominated by the sweeping action of the worm surface but there is also rolling/sliding in the roughly transverse direction due to the motion of the point of contact which is predominantly down the wheel tooth face. A thermal analysis, which takes account of film heating, is essential because of the high degree of sliding present (the slide/roll ratio is approximately 2). In a thermal analysis, which includes solid surface convection (transient surface heating), account must also be taken of the completely different paths of the two surfaces relative to their contact.

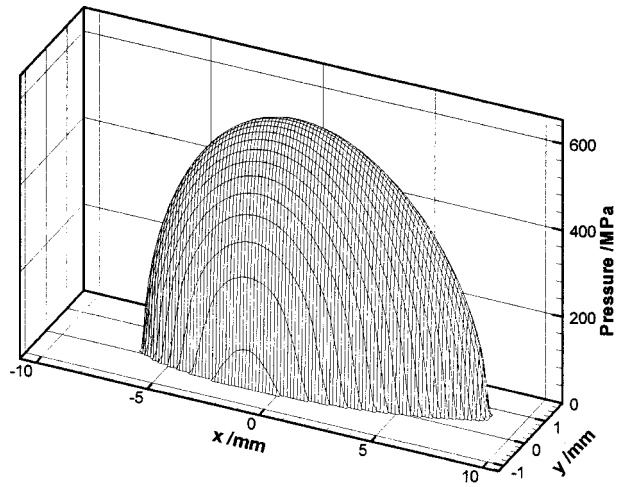

Fig. 4 Pressure distribution for dry contact midway through the meshing cycle

This behavior has important consequences for inlet film heating as will become apparent. These effects, including non-Newtonian lubricant behavior at the high shear rates present, are embodied in a full thermal EHL solver which has been developed for worm contacts.

The flow of oil in an EHL conjunction is due to the motion of the surfaces (Couette flow) and the pressure gradients (Poiseuille flow). In a Newtonian fluid the Poiseuille flow in the axis directions is given by the familiar expressions

$$\frac{\rho h^3}{12\eta}\frac{\partial p}{\partial x}$$

and

$$\frac{\rho h^3}{12\eta}\frac{\partial p}{\partial y}.$$

In a non-Newtonian flow situation, however, the flow in each direction is influenced by both pressure gradients. Consideration of the balance of forces on a small fluid element leads to the conclusion that the shear stress variation across the film must be linear according to

$$\tau_x = \tau_{x_m} + z\frac{\partial p}{\partial x}; \quad \tau_y = \tau_{y_m} + z\frac{\partial p}{\partial y}, \tag{1}$$

and if a rheological model such as that proposed by Johnson and Tevaarwerk [12] is adopted and the shear strain rate components are related to the shear stress components by

$$\frac{\partial U}{\partial z} = \frac{\tau_x}{\tau_e}F(\tau_e)$$

and

$$\frac{\partial V}{\partial z} = \frac{\tau_y}{\tau_e}F(\tau_e) \tag{2}$$

where

$$\tau_e = \sqrt{\tau_x^2 + \tau_y^2}$$

then this coupling of the Pouseille flows is evident.

Recently Morris [13] and Greenwood [14] have shown that the non-Newtonian problem should be formulated in the local sliding (s) and nonsliding (r) directions. The Poiseuille flow can then be expressed as $D\partial p/\partial s$ in the local sliding direction and $C\partial p/\partial r$ in the local nonsliding direction. The flow factors D and C, which are analogous to the term $\rho h^3/12\eta$ that occurs as a multiplier of the pressure gradients in determining Pouiseille flow in a Newtonian Reynolds equation, are intrinsically different so that the effective viscosity is lower in the sliding direction than in the nonsliding direction. Kim and Sadeghi [15] were the first to develop a non-Newtonian solution scheme to the point contact problem based on a modified Reynolds equation, but their formulation failed to recognize that the flow factors are intrinsically different in the sliding and nonsliding directions when conditions depart from Newtonian behavior.

To find the flow factors Eqs. (2) are integrated across the film and nonslip boundary conditions are applied at the solid boundaries. Together with Eqs. (1) this gives a pair of nonlinear equations from which the mid film shear stress components τ_{x_m} and τ_{y_m} may be determined iteratively with a Newton method. The velocity profiles are then integrated numerically to obtain the values of C and D at each point as detailed in Sharif et al. [16].

For the results presented in the current paper the non-Newtonian rheology function $F(\tau_e)$ is that proposed by Bair and Winer [17]

$$\dot{\gamma} = F(\tau) = -\frac{\tau_L}{\eta}\ln(1-\tau/\tau_L) \tag{3}$$

This formulation involves a limiting shear stress τ_L, and τ_e must not exceed this value. This is taken into account in solving Eqs. (1) and (2) for τ_{x_m} and τ_{y_m} with the Newton method being damped when its iteration of τ_{x_m} and τ_{y_m} would lead to τ_e exceeding τ_L in the film. The flow factors D and C thus evaluated are seen to be smoothly varying functions over the EHL solution area and are linearized within the numerical solution scheme. In the worm gear contacts the direction of local sliding varies over the contact area and the Reynolds type equation is required in the global axis set. The flow expressions in the local sliding and nonsliding directions can be resolved to give those in the global axis directions, and the pressure gradient components resolved similarly. This leads to a Reynolds type equation in the global axes that involves cross derivatives of pressure and the angle between the local sliding direction and the global axes.

The basic equations solved in the EHL model are as follows:

(i) Non-Newtonian Reynolds equation:

$$\frac{\partial}{\partial x}\left\{(D\cos^2\phi + C\sin^2\phi)\frac{\partial p}{\partial x}\right\} + \frac{\partial}{\partial y}\left\{(D\sin^2\phi + C\cos^2\phi)\frac{\partial p}{\partial y}\right\} + \frac{\partial}{\partial x}\left\{(D-C)\cos\phi\sin\phi\frac{\partial p}{\partial y}\right\} + \frac{\partial}{\partial y}\left\{(D-C)\cos\phi\sin\phi\frac{\partial p}{\partial x}\right\} = \frac{\partial}{\partial x}(\rho\overline{U}h) + \frac{\partial}{\partial y}(\rho\overline{V}h) \tag{4}$$

The cross derivative terms introduced by the nonconstant sliding direction can be seen to disappear if sliding is in the global axis direction everywhere ($\phi = 0$ Deg or 90 Deg) or if the fluid is Newtonian ($C = D$).

(ii) Viscosity–pressure–temperature relation is that given by Roelands [18]

$$\eta = \eta_0 \exp\left\{(\ln(\eta_0) + 9.67) \times \left[(1 + 5.1\times10^{-9}p)^Z\left(\frac{\theta_0 - 138}{\theta - 138}\right)^{S_0} - 1\right]\right\} \tag{5}$$

where parameters Z and S_0 are taken to be properties of the oil.

(iii) Oil film energy equation

$$\rho c\left(U\frac{\partial\theta}{\partial x} + V\frac{\partial\theta}{\partial y}\right) - \frac{\partial}{\partial x}\left(k\frac{\partial\theta}{\partial x}\right) - \frac{\partial}{\partial y}\left(k\frac{\partial\theta}{\partial y}\right) - k\frac{\partial^2\theta}{\partial z^2} - \varepsilon\left(U\frac{\partial p}{\partial x} + V\frac{\partial p}{\partial y}\right)\theta = \tau_X\frac{\partial U}{\partial z} + \tau_Y\frac{\partial V}{\partial z} \tag{6}$$

(iv) Surface heating equations

$$\theta_S = \theta_{\text{ref}} + \frac{1}{\sqrt{\pi k\rho c}}\int_0^t \frac{q\,d\lambda}{\sqrt{t-\lambda}} \tag{7}$$

(v) Elastic film thickness equation

$$h(x,y) = h_0 + h_u(x,y) + \frac{2}{\pi E'}\int\int_A \frac{p(x',y')}{\sqrt{(x'-x)^2 + (y'-y)^2}}\,dx'\,dy' \tag{8}$$

(vi) Load condition

$$W = \int\int_A p(x,y)\,dx\,dy \tag{9}$$

5 Method of Solution

Equations (4) and (8) are solved within a simple forward type iterative scheme with flow parameters C and D linearized in the outer loop. The energy equation is solved within the iterative scheme by evaluating the right hand side of Eq. (6) in the outer loop together with the coefficient of the θ term. The differential terms in θ are then written in finite difference form using central differences for the conduction terms and backward or forward differences for the convective terms according to the sign of the velocity components $U(z)$ and $V(z)$. The equation is then solved in $\theta(z)$ with the surface temperatures taken as boundary conditions at each point in the mesh by a simple tridiagonal algorithm. During this process the values of $\theta(z)$ at neighboring points are taken to be given by their current approximation. This linearization of temperatures at adjoining positions is found to converge effectively and enables the tridiagonal approach to be adopted at all positions. Where lubricant enters the computing area its temperature is set at the inlet temperature value. This boundary condition applies only to lubricant entering the computing area. The differencing of the convective terms ensures that lubricant leaving the computing region is not subject to a (downstream) boundary condition. Equations of the form of (7) are solved for the surface temperature distribution using the values of $\partial\theta/\partial z$ at the liquid/solid interface to determine the term q in the integrand. For each point on the surface the integral of Eq. (7) is evaluated taking note of the locus of the surface point in reaching its current position so that the time integral is converted into a spatial integral over a curved path determined by the motion of the component relative to the contact point. The two solid surfaces enter the computing region at their specified bulk temperatures and the temperature rise calculated is thus the flash temperature caused by transit through the EHL contact area. The overall solution is obtained when the pressure, film thickness, and temperature fields converge with the constant h_0 in the film thickness equation adjusted to obtain the required load in Eq. (9).

6 Results of EHL Analysis

Typical results of the EHL analysis are shown in Figs. 5–10. The worm design under consideration is a single start 40:1 set

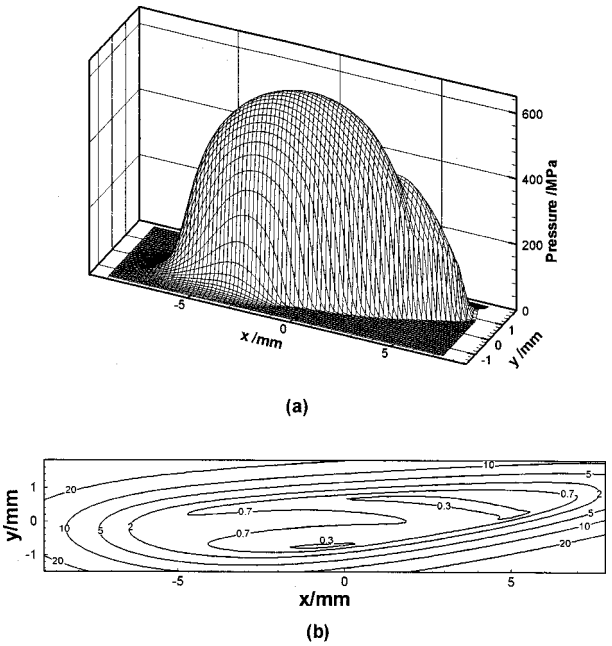

Fig. 5 Results of EHL analysis for case 1 at first $\frac{1}{4}$ point of the meshing cycle: (*a*) pressure surface; (*b*) film thickness contours/μm (inlet is on the left)

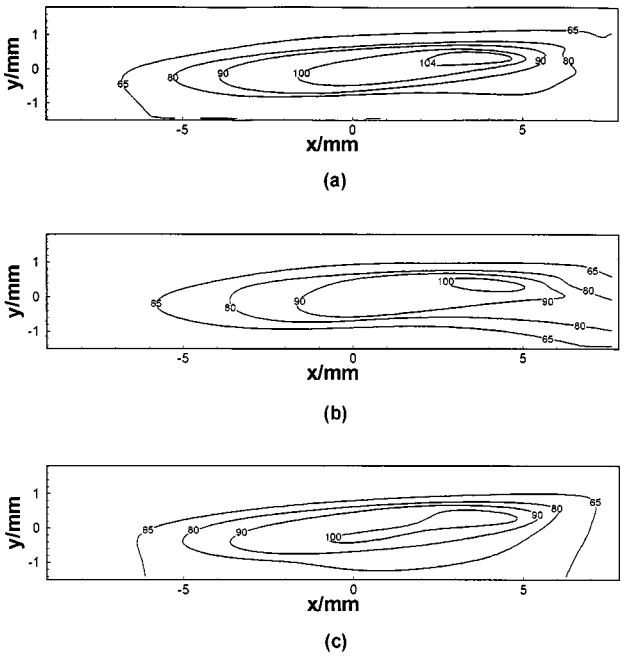

Fig. 6 Temperature contours/°C from EHL solution for case 1: (*a*) mid-film oil temperature; (*b*) worm surface temperature; (*c*) wheel surface temperature

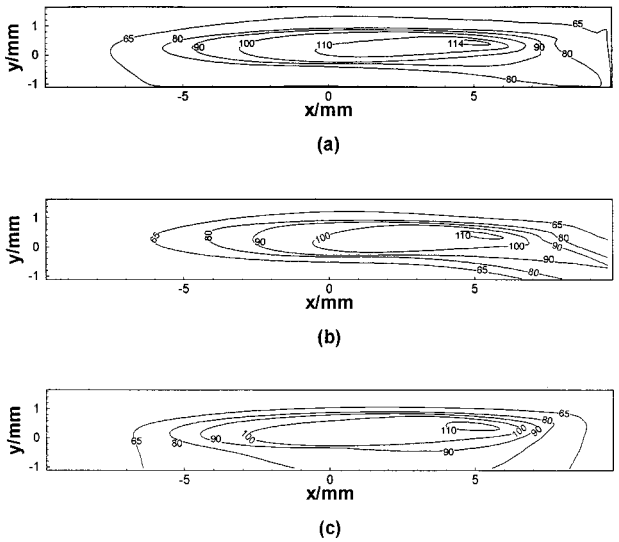

Fig. 8 Temperature contours/°C from EHL solution for case 2: (*a*) mid-film oil temperature; (*b*) worm surface temperature; (*c*) wheel surface temperature

with the design variables given in Table 1. The operating conditions, elastic, rheological, and thermal properties used are given in Table 2. Where properties are taken to be temperature or pressure dependent the expressions used are given in the Appendix. The lubricant modeled is a 460 International Standards Organization viscosity grade polyglycol synthetic gear oil used in an associated experimental project. Lubricant parameter Z was determined by measuring film thickness in an optical interference rig in pure rolling conditions over a range of temperatures and adjusting Z in the numerical model to achieve the same film/speed characteristic. S_0 was determined by measuring the viscosity as a function of temperature. Guidance in specifying these and other lubricant parameters and their possible dependence on pressure or temperature was taken from Larsson et al. [19]. The component velocities are such that the Péclet number ($U\rho ca/2k$) for the worm is $\approx$1000, and that for the wheel is $\approx$5, so that the assumption of linear heat flow leading to Eq. (7) is justified.

The tooth normal load is chosen to give a corresponding peak contact pressure of 600 MPa during the meshing cycle. This represents the typical maximum allowable surface stress when using a steel/bronze combination of materials. Three instantaneous meshing positions are presented. Case 1 is at the first 1/4 point, case 2 is midway through, and case 3 at the last 1/4 point of the meshing cycle. It should be noted that the tooth contact load is assumed to remain constant during the meshing cycle. Considerations of load variation due to load sharing with multiple tooth

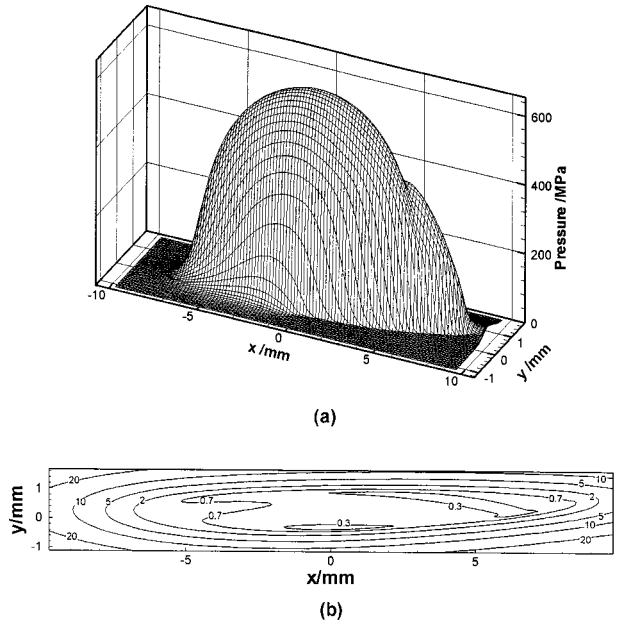

Fig. 7 Results of EHL analysis for case 2 at second 1/4 point of the meshing cycle: (*a*) pressure surface; (*b*) film thickness contours/μm (inlet is on the left)

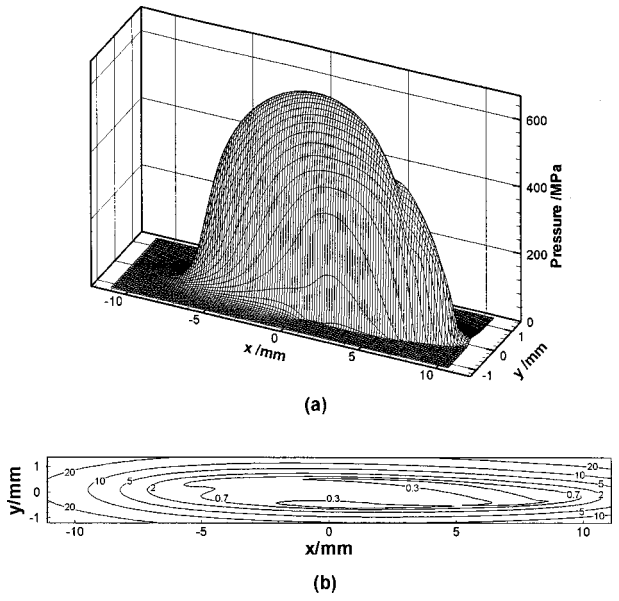

Fig. 9 Results of EHL analysis for case 3 at third 1/4 point of the meshing cycle: (*a*) pressure surface; (*b*) film thickness contours/μm (inlet is on the left)

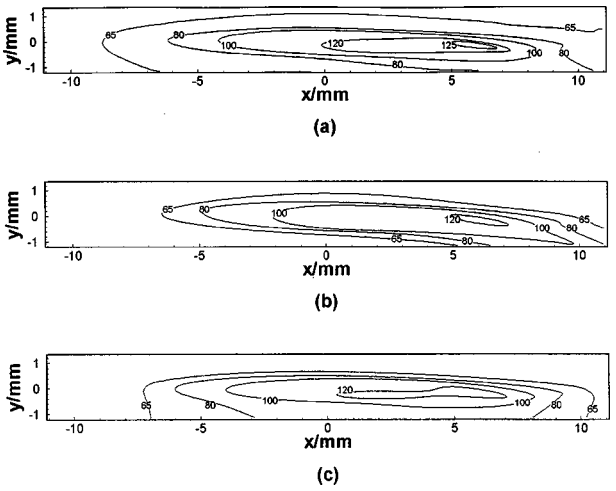

Fig. 10 Temperature contours/°C from EHL solution for case 3: (*a*) mid-film oil temperature; (*b*) worm surface temperature; (*c*) wheel surface temperature

contacts are beyond the scope of this paper. Figure 5 shows the pressure surface and the film thickness contours for case 1. It is seen that there is very little pressure generation outside the dry contact area. The relatively heavily loaded nature of the contact is revealed by the absence of any significant pressure ''spike.'' The main effective inlet to the contact is on the left and along part of the lower edge, although a secondary inlet occurs on the upper part of the contact toward the right. The nonsymmetrical shape of the contours reflects the rolling/sliding/spinning nature of the kinematics. The main features are the regions of thinning in which the film falls to approximately 0.3 μm. The more severe thinning takes place in the upper part of the contact toward the exit region. This is perhaps surprising in view of the fact that the effective entrainment velocity is greater in this region since it corresponds to a larger radius on the worm tooth. A detailed examination of the entrainment velocity pattern over the contact suggests an explanation for this poor film generation however as discussed below. The upper thin film region corresponds to the intersection of the main pressure surface with the shoulder-like pressure feature that extends from it toward the top right of Fig. 5.

Table 2 Worm/wheel operating conditions, material properties, and lubricant properties

Operating Conditions		
Worm input speed / rpm	1500	
Assumed tooth normal load / N	6000	
Maximum contact pressure / MPa	633	
Material Properties		
Parameters	**Worm**	**Wheel**
Modulus of elasticity / GPa	207	120
Poisson's ratio	0.3	0.35
Density / kg/m^3	7900	8800
Thermal conductivity / (W/mK)	47	52
Specific Heat / (J/kgK)	477	420
Lubricant Properties		
Inlet temperature θ_0/ °C	60	
Inlet viscosity η_0/ Pas	0.227	
Inlet density ρ_0/ kg/m^3	1025	
Lubricant parameter Z	0.227	
Lubricant parameter S_0	0.782	
Equivalent pressure viscosity coefficient at 60 °C / GPa^{-1}	9.5	
Limiting shear stress τ_L	maximum of 3MPa, and 0.049p	
Thermal expansivity ε_0/ K^{-1}	7.1x10^{-4}	
Thermal conductivity k_0/ (W/mK)	0.148	
Specific Heat c_0/ (J/kgK)	1844	

Temperature contours for the oil midplane, the worm surface, and the wheel surface are shown in Figs. 6(*a*), 6(*b*), and 6(*c*), respectively. The maximum oil temperature is 105°C which is a rise of 45°C. The worm and wheel surface temperatures are also seen to rise by maximum values of about 40°C. The worm surface sweeps from left to right relative to the contact and there is a buildup of temperature toward the exit as might be expected. The wheel surface moves much more slowly relative to the instantaneous point of contact and in a direction which is nominally perpendicular to that of the worm. The wheel surface as viewed in Fig. 6(*c*) thus moves downward as it passes through the contact receiving heat input. In this case, therefore, the surface temperature tends to build toward the lower part of the contact as shown. This illustrates very clearly the necessity for completely different integration paths in the surface heating equations for the two surfaces. An important consequence of this behavior is that heat, generated by sliding in the contact, is effectively convected back into the primary hydrodynamic inlet of the contact where it contributes to film thinning by reducing the controlling inlet viscosity. This behavior is not generally seen in EHL contacts with linear entrainment in which the inlet is virtually unaffected by transient heating in the main load-bearing region.

Figure 7 shows the EHL pressure distribution and film thickness contours for case 2. The corresponding temperature contours are shown in Fig. 8. Extended thin film regions are again present where the lubricant film falls below 0.3 μm, and the temperature rise is now greater with maximum surface temperatures of 110°C. Figures 9 and 10 show the corresponding results for case 3. The film is now thinner over a larger area of the contact and surface temperatures rise to as much as 120°C. In all of the cases the shoulder feature seen to the top right of the pressure illustration joins the ''main'' pressure distribution at the location of the thin extended upper thin film region of the contact.

For the worm design considered the transmitted power at the tooth contact is 2930 W. The instantaneous power loss due to fluid shear in the mesh is calculated as 239 W for case 1, 295 W for case 2 and 362 W for case 3, giving predicted instantaneous mesh efficiency figures of 92 percent, 90 percent, and 88 percent, respectively.

7 Possible Prediction of Film Thinning from Kinematics

It is a feature of heavily loaded side-leakage EHL conjunctions that the constrictions that are seen in the main Hertzian part of the contact are due to sideways leakage of the lubricant in the inlet section. Flow within the thin film/high pressure part of the contact is almost entirely due to the motion of the surfaces (Couette flow) because the film is very thin and the viscosity very high. The pressure–flow (Poiseuille flow) is therefore stifled, and oil which is entrained over the edge of the contact effectively follows the entrainment direction within the contact. This physical understanding, when applied to a typical worm contact, reveals some interesting behavior which may explain the results shown in Figs. 5–10. Figure 11 shows the edge of the dry contact between worm teeth corresponding to Fig. 7 together with the entrainment vectors arising from the meshing action. From this figure it is clear that the contact has, effectively, two inlet regions. The first inlet is on the lower left edge of the contact. Some of the oil entrained in this inlet is carried through the contact and emerges to the lower

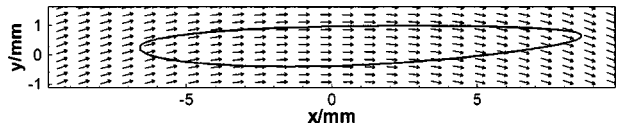

Fig. 11 Area of dry elastic contact for case 2 showing entrainment velocity vectors

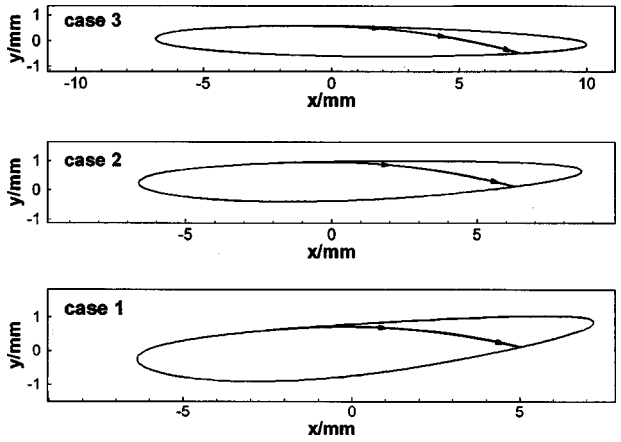

Fig. 12 Line of predicted poor film generation for cases 1, 2, and 3

right edge and some leaves on the upper left boundary. A second inlet occurs on the upper right edge and oil is carried through the contact to emerge on the lower right. This process divides the overall contact into two separate regions each with its own inlet and exit. The border between these two areas is effectively a line of zero entrainment because it is tangential to the upper edge of the contact at a point where oil neither enters nor leaves the contact. This border is illustrated for each of the three cases in Fig. 12. The line has been drawn by manually locating the point on the edge of the contact at which the entrainment vectors become tangential. The line then follows the entrainment streamline. The lines, when superimposed on the EHL film contour maps shown in Figs. 5, 7, and 9, coincide with the edge of the narrow area of extreme thinning in the upper right of the contact.

8 Discussion

The central and minimum film thickness values calculated for the three cases are given in Table 3. The model was also evaluated using isothermal conditions with the non-Newtonian lubricant model, and also with a Newtonian isothermal model. Corresponding film thickness values for these models for each case are also included in Table 3. The film thickness values obtained are compared with estimates made by use of the formulas presented by Chittenden et al. [20] for elliptical contacts with entrainment at any angle to the ellipse axes. These formulas were used in two ways: first using the entraining velocity at the contact point together with the principal radii of relative curvature at the same location (denoted $CDDT_1$), and second taking the entrainment angle to be that at the inlet edge of the corresponding dry contact (denoted $CDDT_2$). The formulas of Chittenden et al. are based on Newtonian isothermal conditions and so the most appropriate comparison is with the results for that model. It should also be noted that the radius ratios $R_x/R_y = 29$, 38, and 62 for the three cases are outside the range considered in deriving the formulas.

The more elongated region of thinning in the upper part of the contact (compared to that in the lower part) appears to be due to poor entrainment conditions at the edge of the contact where the rolling vector is parallel to the edge. Due to the motion of the contact over the wheel tooth the two thin film regions sweep out a significant area on the tooth during the meshing cycle, and indeed this is the location of the heaviest wear. It would be desirable to avoid this condition if possible, but it remains to be seen if this can be achieved by suitable changes to the worm design parameters. Clearly, any changes that lead to a greater degree of entrainment across rather than along the contact would be beneficial. A further factor which leads to film thinning is the unusual thermal behavior whereby the wheel surface, after being heated in the contact, moves into the primary hydrodynamic inlet to the contact. This tends to exacerbate the shear heating in the inlet caused by sliding. These factors may contribute to the observed poor lubrication performance of worms. It is hoped that on the basis of a more thorough understanding of EHL effects it will be possible to improve worm gear performance.

The predicted efficiencies for the three conditions considered are based on the nominal expression for τ_L adopted for this investigation. They are somewhat higher than that measured in experiments with worm gear sets. This is expected as surface roughness and load sharing effects are ignored. The efficiency figures relate to instantaneous mesh friction only and make no allowance for windage or any other losses. The geometry of steel/bronze worm gear contacts is subject to continuous modification by the ''bedding in'' of the bronze wheel, a process that will invariably lead to mixed lubrication conditions. The analysis included in the current paper refers to the unmodified smooth surface geometry as manufactured.

9 Conclusion

Dry elastic contact simulation has been used to reveal the true area of contact and contact stresses occurring between worm gear teeth under load. A full EHL analysis predicts a region of severe thinning of the oil film which, on the basis of a physical understanding of the EHL mechanism, appears to be caused by the kinematics of the contact leading to a line of zero entrainment which effectively divides the overall contact into two separate regions.

Table 3 Central and minimum film thickness values

	Case 1		Case 2		Case 3	
Model	h_c / μm	h_m / μm	h_c / μm	h_m / μm	h_c / μm	h_m / μm
Thermal, non-Newtonian	0.74	0.21	0.60	0.18	0.47	0.11
Isothermal, non-Newtonian	0.94	0.24	0.80	0.24	0.67	0.19
Isothermal Newtonian	1.02	0.30	0.89	0.31	0.77	0.26
$CDDT_1$	0.48	0.23	0.47	0.22	0.43	0.20
$CDDT_2$	0.57	0.28	0.53	0.26	0.57	0.28

Acknowledgments

The authors acknowledge the assistance of Dr. J. Hu and A. Pennell of Newcastle University in providing the geometry analysis software used in this project and also for many helpful discussions. The authors are also grateful for the financial support provided by EPSRC Grant No. GR/L 69824 and for further financial support by the British Gear Association (http://www.bga.org.uk).

Nomenclature

a = contact semidimension m
A = area subject to lubricant pressure m^2
c = specific heat J/kg K
C, D = flow factors in non-Newtonian Reynolds equation ms
E' = reduced elastic modulus Pa
h = film thickness m
h_0 = load determining constant in film thickness equation m
h_u = undeformed film shape m
k = thermal conductivity W/mK
p = pressure Pa
q = heat flux at solid boundary W/m^2
r = coordinate in the local nonsliding direction m
s = coordinate in the local sliding direction m
t = time of heating s
U = fluid velocity in the x direction m/s
V = fluid velocity in the y direction m/s
$\overline{U}$ = mean surface velocity in the x direction m/s
$\overline{V}$ = mean surface velocity in the y direction m/s
W = load N
x = Cartesian coordinate in contact plane m
y = Cartesian coordinate in contact plane m
z = coordinate perpendicular to contact plane m
ε = oil thermal expansivity K^{-1}
ϕ = angle between x and s directions
$\dot{\gamma}$ = shear strain rate s^{-1}
λ = dummy variable in surface temperature integral s
μ = absolute viscosity Pa s
θ = temperature K
θ_0 = reference temperature for viscosity relationship K
θ_{ref} = bulk temperature of component K
θ_s = surface temperature of component K
ρ = density kg/m^3
τ = shear stress Pa
τ_L = limiting shear stress Pa
τ_x, τ_y = Shear stress in x and y directions Pa
τ_{x_m}, τ_{y_m} = Shear stress in x and y directions at oil mid film Pa

Appendix: Lubricant Properties Assumed in the Analysis

Lubricant properties are pressure and/or temperature dependent according to the following formulas. Suffix 0 represents the value at zero pressure and reference temperature θ_0

$$\frac{\rho(p,\theta)}{\rho_0} = \left(1 + \frac{D_1 p}{1 + D_2 p}\right)(1 - \varepsilon(\theta - \theta_0))$$

where $D_1 = 0.67\ \mathrm{GPa}^{-1}$ and $D_2 = 2.68\ \mathrm{GPa}^{-1}$

$$\varepsilon = \varepsilon_0 e^{-\lambda p}$$

where $\lambda = 1.5\ \mathrm{GPa}^{-1}$

$$k = k_0\left(1 + \frac{C_1 p}{1 + C_2 p}\right)$$

where $C_1 = 1.56\ \mathrm{GPa}^{-1}$ and $C_2 = 0.61\ \mathrm{GPa}^{-1}$

$$c(p,T) = \frac{\rho_0}{\rho} c_0\{1 + b_0(1 + b_1 p + b_2 p^2)(\theta - \theta_0)\}\left(1 + \frac{K_1 p}{1 + K_2 p}\right)$$

where $b_0 = 3.4 \times 10^{-4}$, $b_1 = 3.3\ \mathrm{GPa}^{-1}$, and $b_2 = -2.3\ \mathrm{GPa}^{-2}$, and $K_1 = 0.5\ \mathrm{GPa}^{-1}$ and $K_2 = 0.51\ \mathrm{GPa}^{-1}$.

References

[1] Britton, R. D., Elcoate, C. D., Alanou, M. P., Evans, H. P., and Snidle, R. W., 2000, ''Effect of Surface Finish on Gear Tooth Friction,'' Trans. ASME, J. Tribol., **122**, pp. 354–360.
[2] Litvin, F. L., and Kin, V., 1992, ''Computerised Simulation of Meshing and Bearing Contact for Single-Enveloping Worm-Gear Drives,'' Trans. ASME J. Mech. Design, **114**, pp. 313–316.
[3] Seol, I. H., and Litvin, F. L., 1996, ''Computerised Design, Generation and Simulation of Meshing and Contact of Modified Involute, Klingelnberg and Flender Type Worm-Gear Drives,'' Trans. ASME, J. Mech. Design, **118**, pp. 551–555.
[4] Fang, H., and Tsay, C., 1996, ''Mathematical Model and Bearing Contacts of the ZK-Type Worm Gear Set Cut by Oversize Hob Cutters,'' Mech. Mach. Theory, **31**, pp. 271–282.
[5] Hu, J., 1997, ''The Kinematic Analysis and Metrology of Cylindrical Worm Gearing,'' PhD thesis, University of Newcastle upon Tyne, England.
[6] Su, D., Yang, F., and Gentle, C. R., 1998, ''A New Approach Combining Numerical Analysis and Three Dimensional Simulation for Design of Worm Gearing with Preferable Localized Tooth Contact,'' *Proc. ASME Design Engineering Technical Conference*, Atlanta, GA, pp. 1–9.
[7] Bathgate, J., and Yates, F., 1970, ''The Application of Film Thickness, Flash Temperature and Surface Fatigue Criteria to Worm Gears,'' ASLE Trans., **13**, pp. 21–28.
[8] Fuan, C., Chen, Z., Yeuhai, S., and Jing, S., 1998, ''Lubrication Basis Theory of Worm Pair and Temperature Distribution on Worm Gear Surface,'' Chin. J. Mech. Eng., **11**, pp. 19–22.
[9] Simon, V., 1985, ''Thermoelastohydrodynamic Analysis of Lubrication of Worm Gears,'' *Proc. JSLE International Tribology Conference*, JSLE, Tokyo, Japan, pp. 1147–1152.
[10] Simon, V., 1997, ''EHD Lubrication Characteristics of a New Type of Ground Cylindrical Worm Gearing,'' Trans. ASME, J. Mech. Design, **119**, pp. 101–107.
[11] Snidle, R. W., and Evans, H. P., 1994, ''A Simple Method of Elastic Contact Simulation,'' Proc. Inst. Mech. Eng., Part J., **208**, pp. 291–293.
[12] Johnson, K. L., and Tevaarwerk, J. L., 1977, ''The Shear Behavior of Elastohydrodynamic Oil Films,'' Proc. R. Soc. London, Ser. A, **356**, pp. 215–236.
[13] Morris, S. J., 2000, ''Traction in Elliptical Point Contacts,'' Ph.D. thesis, University of Wales, Cardiff, Wales.
[14] Greenwood, J. A., 2000, ''Two-Dimensional Flow of a Non-Newtonian Lubricant,'' Proc. Inst. Mech. Eng., Part J, **214**, pp. 29–41.
[15] Kim, K. H., and Sadeghi, F., 1991, ''Non-Newtonian Elastohydrodynamic Lubrication of Point Contact,'' Trans. ASME, J. Tribol., **113**, pp. 703–711.
[16] Sharif, K. A. H., Kong, S., Evans, H. P., and Snidle, R. W., 2000, ''Non-Newtonian Thermal Elastohydrodynamic Analysis of Worm Gear Contacts: Part 1 Theoretical Formulation; Part 2 Results,'' Proc. Inst. Mech. Eng., Part C: Mech. Eng. Sci. (submitted).
[17] Bair, S., and Winer, W. O., 1979, ''A Rheological Model for Elastohydrodynamic Contacts Based on Primary Laboratory Data,'' Trans. ASME J. Lubr. Technol., **101**, pp. 258–265.
[18] Roelands, C. J. A., 1966, ''Correlation Aspects of the Viscosity-Temperature-Pressure Relationship of Lubricating Oils,'' PhD thesis, Technical University Delft, The Netherlands, (V. R. B. Gronigen, The Netherlands).
[19] Larsson, R., Larsson, P. O., Eriksson, E., Sjöberg, M., and Höglund, E., 2000, ''Lubricant Properties for Input to Hydrodynamic and Elastohydrodynamic Lubrication Analyses,'' Proc. Ins. Mech. Eng., Part J, **214**, pp. 17–28.
[20] Chittenden, R. J., Dowson, D., Dunn, J. F., and Taylor, C. M., 1985, ''A Theoretical Analysis of the Isothermal Elastohydrodynamic Lubrication of Concentrated Contacts,'' Proc. R. Soc. London, Ser. A, **397**, pp. 271–294.